Equilibrium structure and deformation response of 2D kinetoplast sheets

Alexander R. Klotz[a,b], Beatrice W. Soh[a], and Patrick S. Doyle[a,1]

[a]Department of Chemical Engineering, Massachusetts Institute of Technology, Cambridge, MA 02142; and [b]Department of Physics and Astronomy, California State University, Long Beach, CA 90840

Edited by Steve Granick, Institute for Basic Science, Ulju-gun, Ulsan, Korea (South), and approved November 1, 2019 (received for review August 2, 2019)

The considerable interest in two-dimensional (2D) materials and complex molecular topologies calls for a robust experimental system for single-molecule studies. In this work, we study the equilibrium properties and deformation response of a complex DNA structure called a kinetoplast, a 2D network of thousands of linked rings akin to molecular chainmail. Examined in good solvent conditions, kinetoplasts appear as a wrinkled hemispherical sheet. The conformation of each kinetoplast is dictated by its network topology, giving it a unique shape, which undergoes small-amplitude thermal fluctuations at subsecond timescales, with a wide separation between fluctuation and diffusion timescales. They deform elastically when weakly confined and swell to their equilibrium dimensions when the confinement is released. We hope that, in the same way that linear DNA became a canonical model system on the first investigations of its polymer-like behavior, kinetoplasts can serve that role for 2D and catenated polymer systems.

polymers | 2D materials | molecular topology

Two-dimensional (2D) materials have been an active area of research since the discovery of graphene in 2004 (1). Investigations have typically focused on the electronic properties of crystalline materials, but the desire for stretchable and wearable electronics as well as versatile membranes for chemical separation and optoelectronics has shifted interest toward 2D soft materials (2). In the same manner that the materials industry in the 20th century was revolutionized by the advent of linear polymers, 2D polymers may serve an equivalently important industrial role in the 21st century. Methods exist to synthesize macromolecules with a planar architecture (3), which must be complemented with an understanding of 2D polymer statistics. Beyond the chemistry of planar synthesis, a model system is desired to explore the underlying physics of 2D polymers. Exfoliated graphene has been explored as a model system for 2D polymer rheology (4), but it has strong size polydispersity and is not sufficiently large for single-sheet analysis.

Single-molecule investigation reveals subtlety in polymer dynamics that is lost through ensemble-average techniques and serves a vital role in connecting molecular-scale behavior to bulk material properties (5, 6). The behavior of 2D polymers on the single-molecule level is expected to be qualitatively and quantitatively different from 1D polymers, but due to the lack of complementary mesoscale experimental systems, their statistical scaling behavior and the nature of their phase transitions are not well understood (7). For example, controversy exists in the 2D polymer literature over the existence of a transition from a membrane-like flat phase to a crumpled phase (8, 9). A single-molecule system that could embody the mechanics of elastic sheets and the statistics of 2D polymers at visible-microscopy length scales is desirable.

Single-molecule studies using genomic DNA have revolutionized the field of polymer physics in the past two decades and have established DNA as the canonical semiflexible polymer (10–14). The utility of viral DNA in this role stems not only from its monodispersity and the existence of dyes and optics for its visualization but also, from its widespread commercial availability. Recent experimental studies have expanded the use of DNA to study polymers with nontrivial topology, including rings (15–18), branched chains (19), and knots (20, 21). There are more complex molecular topologies that are difficult to achieve without advanced synthetic methods, including polyrotaxanes (shish kebab molecules) and polycatenanes (linked rings) (22). Chemistry based on DNA–protein enzymatic reactions has been demonstrated to generate "Olympic gels" by linking circular molecules together (23, 24), demonstrating the utility of DNA as a tool for studying catenated materials.

To understand the physics of 2D polymers as well as those of catenated systems, it is desirable to have a model experimental system that fills the same roles as genomic DNA has for linear polymers. Such a system does exist in the form of the kinetoplast.

A kinetoplast is a DNA structure found in the mitochondria of trypanosome parasites, including those responsible for human diseases such as sleeping sickness and Leishmaniasis (25). Unique among organismal DNA, the kinetoplast is composed of thousands of small loops of DNA (minicircles), roughly 200 nm in diameter, that are topologically interconnected like chainmail rings in a 2D catenated network (26) (Fig. 1*A*). Within that network, there are additionally several dozen larger rings (maxicircles) containing the mitochondrial genome. The biological role of this structure is convoluted: the mitochondrial genes from the maxicircles transcribe encrypted messenger RNA (mRNA), and the minicircles are transcribed into a "guide" RNA that edits the mitochondrial mRNA sequence to allow translation. It

Significance

We study the polymer physics of complex DNA networks called kinetoplasts, membrane-like structures consisting of thousands of rings connected together like chainmail, found in the mitochondria of parasites that cause tropical diseases, such as Leishmaniasis. We make observations of individual kinetoplasts in solution to measure their equilibrium properties, finding that kinetoplasts adopt a hemispherical configuration with strong intrinsic curvature, which undergoes small-amplitude fluctuations at subsecond timescales, and can stretch and compress elastically in confinement. We anticipate that our findings will establish kinetoplasts as a model system for single-molecule studies of topologically complex 2-dimensional polymer systems.

Author contributions: A.R.K. and P.S.D. designed research; A.R.K. and B.W.S. performed research; A.R.K. analyzed data; and A.R.K. and P.S.D. wrote the paper.

The authors declare no competing interest.

This article is a PNAS Direct Submission.

Data deposition: The data reported in this paper have been deposited in the Harvard Dataverse public repository, https://doi.org/10.7910/DVN/I4TWFV.

See Commentary on page 18.

[1]To whom correspondence may be addressed. Email: pdoyle@mit.edu.

This article contains supporting information online at https://www.pnas.org/lookup/suppl/doi:10.1073/pnas.1911088116/-/DCSupplemental.

First published December 6, 2019.

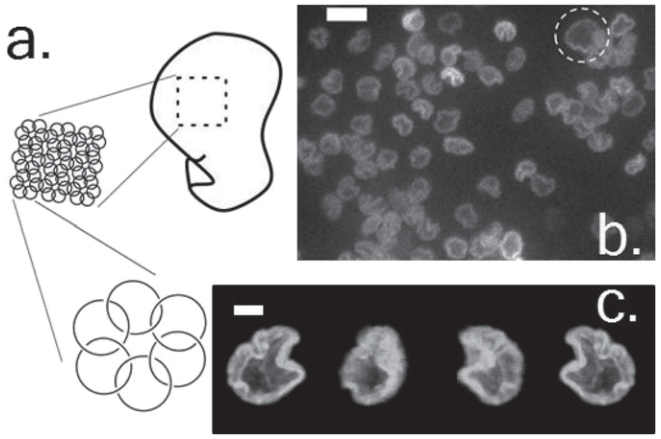

Fig. 1. (*A*) Schematic diagram of a kinetoplast, a curved sheet-like structure made of thousands of connected rings of DNA. (*B*) Fluorescence microscopy image of a population of *C. fasciculata* kinetoplasts in solution. The dashed circle indicates a larger kinetoplast that has undergone replication. (Scale bar: 10 μm.) (*C*) Confocal image of a single kinetoplast displayed at 4 angles, with a wrinkled hemispherical appearance. (Scale bar: 2 μm.)

is believed that the rings are contained in a catenated network in order to ensure that dividing cells have all of the necessary minicircles (27). Outside the realm of parasitology, limited mathematical investigation into kinetoplasts has focused on their network topology (28, 29), but to the authors' knowledge, there has been no investigation of their material properties.

The addition and removal of linked DNA in a network are facilitated by topoisomerases, a family of enzymes that can change the topology of DNA, are vitally important for cell division, and are adversely expressed in certain cancers (24). Assays for ascertaining the presence and function of topoisomerase are necessary for biomedical research, and such assays require a DNA substrate that has a highly mutable topology. Kinetoplasts from *Crithidia fasciculata*, a parasite that infects mosquitoes, are commercially available from multiple companies for this purpose. The field of single-DNA polymer physics was made possible in part due to the commercial availability of viral DNA, and it is fortuitous that we as physicists and engineers can study kinetoplast DNA without the need to culture parasites and mosquitoes or to synthesize molecules.

Here, we report on the equilibrium properties and deformation response of individual *Crithidia* kinetoplasts in solution (30). We observe that, in good solvent conditions, the kinetoplasts appear as an extended hemispherical sheet, which can undergo small-scale thermal fluctuations with a subsecond timescale. Principal component analysis (PCA) is used to show that, while the ensemble average shape of a kinetoplast can be approximated by a hemisphere with a diameter of ∼5 μm, each kinetoplast appears to have a unique conformation, presumably related to subtle differences in topology. We further show that kinetoplasts behave like elastic sheets, which can reversibly fold and unfold in microfluidic deformation assays.

Results and Discussion

Kinetoplasts have primarily been imaged within cells or flattened onto surfaces for scanning electron microscopy (SEM) (26) or atomic force microscopy (AFM) (31). In the cell, they appear as a tight disk, and they appear as a flat ellipsoid on surfaces. We report on the qualitative appearance of kinetoplasts in solution, where we can image many of them at population scales (in contrast to SEM and AFM imaging) and can observe their dynamics at equilibrium. A population of fluorescently stained *Crithidia* kinetoplasts can be seen in Fig. 1*B*. In projection, they have a roughly floral appearance and a diameter near 5 μm. There is a region of excess intensity around the edge of the kinetoplasts, likely corresponding to the thick fibril seen in SEM studies (32). While there is qualitative variation in their wrinkled outline, they have good monodispersity with respect to size. A small subpopulation of kinetoplasts has been doubled in size by the cell's replication mechanism (33), an example of which is circled in Fig. 1*B*. Examining kinetoplasts in three dimensions using confocal microscopy (Fig. 1*C*) reveals that, despite their 2D topology, the networks have significant curvature and have a hemispherical shape not dissimilar to a jellyfish bell, with significant wrinkling and a lip at their opening.

More quantitative data about the 3-dimensional structure of kinetoplasts are seen in Fig. 2. Fig. 2*A* shows two projections of a kinetoplast: one projecting the "cup" onto the image plane and viewed from the top, and the other viewed from the side. To characterize the dimensions of the kinetoplast, we compute the gyration tensor in three dimensions from confocal data and find its principal eigenvalues, corresponding to the length of the three perpendicular axes. The shape can be simply described as a wrinkled bowl with an elliptical cross-section, where the smallest axis corresponds to the depth of the bowl and the second and third correspond to the minor and major diameters of the opening, respectively. This is confirmed by examining by eye kinetoplasts with principal eigenvectors that are close to the orthogonal axes of the pixel grid and the confocal *z* stack. Histograms of all three axes are seen in Fig. 2*B*, where notable outliers in the major axis data represent kinetoplasts that have

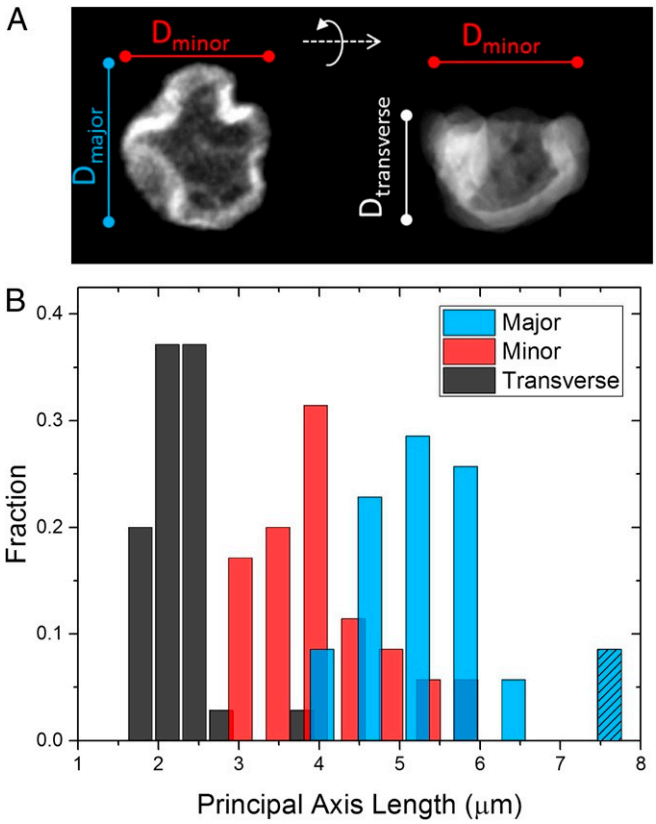

Fig. 2. (*A*) Projection of a confocal kinetoplast image onto the *xy* and *xz* planes showing the in-plane major and minor axes and the out-of-plane transverse axis as determined from the eigenvectors of the 3 × 3 intensity-weighted gyration tensor. (*B*) Histograms of the three principal axes for a population of 31 kinetoplasts imaged with confocal microscopy. The major axis outliers (hatched) are a small subpopulation of replicated networks.

been duplicated as part of the cell replication cycle (33). We note that duplicated kinetoplasts are typically flatter than the standard ones, suggesting that the observed curvature emerges during or after network cleavage. The means of the principal diameters of the population, neglecting duplicated kinetoplasts, are 2.86 ± 0.06, 4.16 ± 0.10, and 5.53 ± 0.10 μm (all SE). The major axis of the duplicated kinetoplasts is 7.7 ± 0.4 μm (SE), a factor of near $\sqrt{2}$ greater than the interphase population, suggesting that they do indeed contain twice the number of minicircles. Additional exploration of the equilibrium dimensions of duplicated kinetoplasts may substantiate theoretical models of 2D polymer scaling laws.

While the sizes of kinetoplasts show strong monodispersity, there is significant variation in their visual appearance, with some appearing as nearly circular ellipsoids and others with intricate edge curvature (Fig. 3*A*). To interrogate their morphology, we studied kinetoplasts that were weakly confined in microfluidic channels with the height of 2 μm, comparable in height with their transverse axis. This confinement is not sufficiently strong to deform them, but orients them with their "opening" in the plane of channel and with their "lip" forming a continuous bright outline. We can characterize their shape by using an edge detection algorithm to find the polar coordinates of the outline, described in greater detail in *SI Appendix*. A sample of edge coordinates from a population of 136 kinetoplasts was analyzed using PCA to determine the most important contributors to their shapes. The principal components (PCs) have appearances similar to deformed harmonic modes (Fig. 3*B*). A vector in the 72-dimensional PC space points uniquely to each kinetoplast outline, and a pair of PCs will separate the population adequately with some overlap. The PCs are ordered by the amount of variance among the population. The population varies the most in the "heart-shaped" modes (PC1 and PC2), but higher-order modes are required to encapsulate the more complex fine structures of the edge. Fig. 3*C* shows the outline of an intricate kinetoplast constructed with 3, 6, and 9 amplitudes. The first three modes are insufficient for constructing the detailed outline of the molecule, while the finer features are captured with 6. To show the variation in edge shape across the ensemble, we plot the locations of each kinetoplast in the PC1–PC2 axes (Fig. 3*D*) and show plots for PC3–PC4 and PC5–PC6 in *SI Appendix*. Images of several kinetoplasts are shown on this plot, corresponding to the red data points in Fig. 3*D*. The example near the center of the distribution appears elliptical, while those farther to edges have more intricate outlines. Representing kinetoplasts by their PCs allows a systematic separation in space that verifies what we see by eye: that there are significant differences between the shapes of kinetoplasts. The amplitudes along each of the PCs are by definition uncorrelated, but it is possible for certain types of kinetoplasts to cluster together. This is not evident by eye; to ascertain whether the PC data were clustered into different subpopulations, we used *k*-means clustering on pairwise combinations of the first 20 PCs and triplet combinations of the first 10, and evaluated the gap statistic (34) to determine whether 2 or 3 clusters were appropriate compared with the null assumption of a single cluster. We found no evidence of clustering in the population.

We surmise that the unique appearance and PC coordinates of each kinetoplast are due to the topology of its underlying network connectivity. Because this topology is fixed in the absence of strand breakages, we expect that the appearance of each kinetoplast should remain similar over longer timescales and that its location in PC should remain localized. We confirm visual similarities in kinetoplasts imaged every 5 min for half an hour, 4 orders of magnitude longer than their fluctuation timescale (Fig. 3*E*), and examine their trajectory in PC space (Fig. 3*D*). While there is movement across this space, it is small relative to the observed variation in the population. There may be overlap in the PC1–PC2 locations of some kinetoplasts, but greater localization can be found in higher-dimensional representations of PC amplitudes. We show "spider plots" of kinetoplasts across the first 6 components in *SI Appendix*.

The bright edge of the kinetoplast is likely due to the "fibril" that has been seen in electron microscopy studies (35). The fibril is made of many redundantly catenated parallel loops that

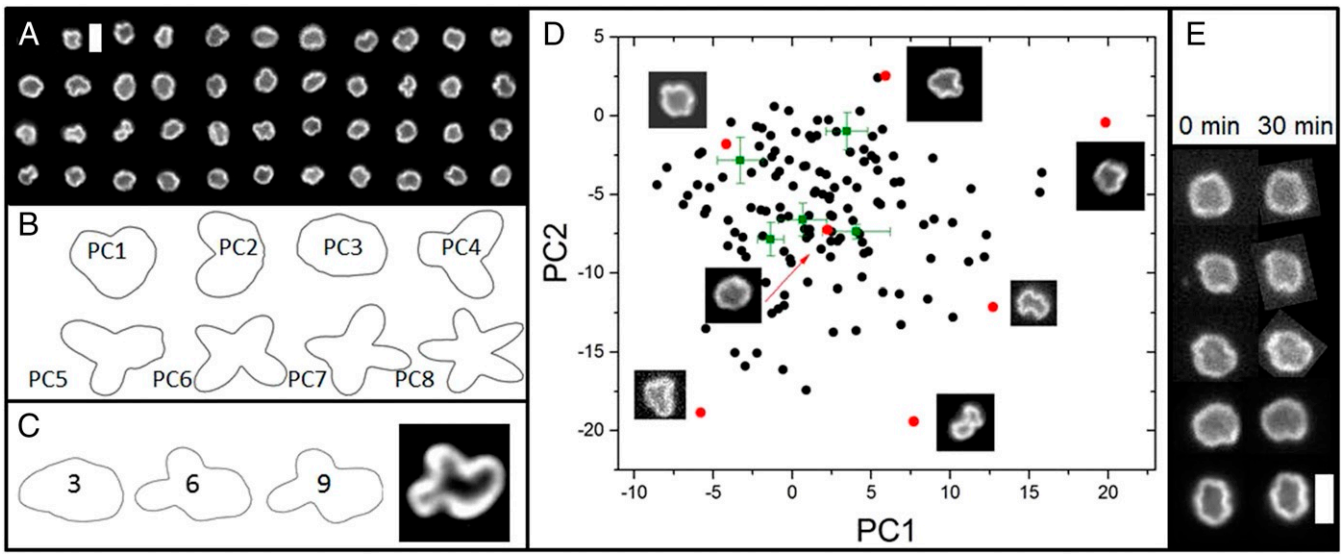

Fig. 3. PCA of kinetoplast edge shapes. (*A*) A subset of 43 of 136 confined kinetoplasts that make up our ensemble used for edge analysis. (Scale bar: 5 μm.) (*B*) Images of the first 8 PCs that are calculated from the polar edge coordinates of our ensemble. (*C*) Reconstruction of a kinetoplast with a complex edge from its PC amplitudes. Plots show the outline constructed from the first 3, 6, and 9 amplitudes. (*D*) Scatter plot of the first and second PC amplitudes for the 136-kinetoplast ensemble. Images are shown for select kinetoplasts throughout PC space (red points). Green points correspond to kinetoplasts observed over longer timescales at 5-min intervals, with the error bars representing the SD between the time points. (*E*) Five kinetoplasts observed half an hour apart, corresponding to the green points in the scatter plot. Their shapes appear visually unchanged, and their PC magnitudes stay localized in PC space. (Scale bar: 5 μm.)

form a repeating "rosette" pattern. The relationship between the fibril, the curvature of the network, and its overall connectivity is not fully known, nor is the causative relationship between the geometric shape of the fibril and the overall structure of the kinetoplast. It has been estimated based on restriction enzyme digestion that the topology of a kinetoplast network is that of a honeycomb lattice, with each loop connected to 3 others (36). A more recent study has estimated a spectrum of topologies but still is based around regular lattice structures (29). Another computational study suggests that the connectivity is such that the network is barely percolated (28). Our observations of the diversity of apparent shapes and their long time-stable nature suggest to us that there is a broad spectrum of network connectivities that varies significantly from one kinetoplast to the next. We posit that the lattice picture is overly simplistic and that the role of the edge fibril has been underestimated in determining the apparent shape of the network. The observation of kinetoplast network "individualism" suggests biophysical analyses to ascertain the underlying topology.

While their shape does not significantly evolve over time, they undergo dynamic fluctuations at short timescales. For a linear polymer, the dominant timescale is that of conformational decorrelation, which is equivalent to the timescale over which a polymer diffuses a distance equivalent to its radius of gyration, as well as its stretch-relaxation timescale (37). For a 2D kinetoplast, these timescales are not necessarily equivalent, and the fixed topology restricts the conformational space. Over short periods of time, the kinetoplasts are observed to undergo small shape fluctuations (Movie S1). The kinetoplasts are observed to undergo translational and rotational diffusion, albeit slowly, taking several minutes to diffuse their own diameter or rotate completely.

To quantify the dynamics of the kinetoplasts, we study the in-plane anisotropy, ϵ, defined as the ratio between the minor and major axes. We calculate the autocorrelation function $A(\Delta t)$ of the kinetoplast's anisotropy:

$$A(\Delta t) = \frac{1}{\sigma_\epsilon^2 T} \sum_{t=1}^{T-\Delta t} (\epsilon(t) - \bar{\epsilon})(\epsilon(t+\Delta t) - \bar{\epsilon}), \qquad [1]$$

where ϵ is measured over T camera frames, $\bar{\epsilon}$ is the average value over a given time series, and σ_ϵ^2 is the sample variance. An example time series of the anisotropy is seen in Fig. 4*A*, and an ensemble of autocorrelation functions and their mean is seen in Fig. 4*B*, with data recorded at 50 frames per second. The autocorrelation function of an individual kinetoplast anisotropy is very quickly decaying at short timescales and has a longer-time tail. The population-averaged fast timescale was found to be 0.216 ± 0.004 s (SE), comparable with that of the much smaller linear λ-DNA (48 kbp compared with ~12 Mbp of a kinetoplast). The longer-time tail has an ensemble-averaged characteristic timescale of 6.5 ± 0.1 s (SE), although this may vary between kinetoplasts (Fig. 4*B*) and is the result of microfluidic confinement and out-of-plane effects. The kinetoplasts are weakly confined in the microfluidic channels, which orient the kinetoplasts in the same plane and suppress out-of-plane rotation without significantly deforming them. Small-amplitude partial out-of-plane rotations increase the apparent correlation time of the kinetoplast's shape fluctuations, and interactions of the kinetoplast edge with the wall can lead to isolated changes in the anisotropy. A discussion of these effects can be found in *SI Appendix*.

Microfluidic and nanofluidic confinements are often used to investigate the mechanical response of soft objects and single polymers through experiments, such as the nanochannel confinement assay (38–40) and the microfluidic constriction assay

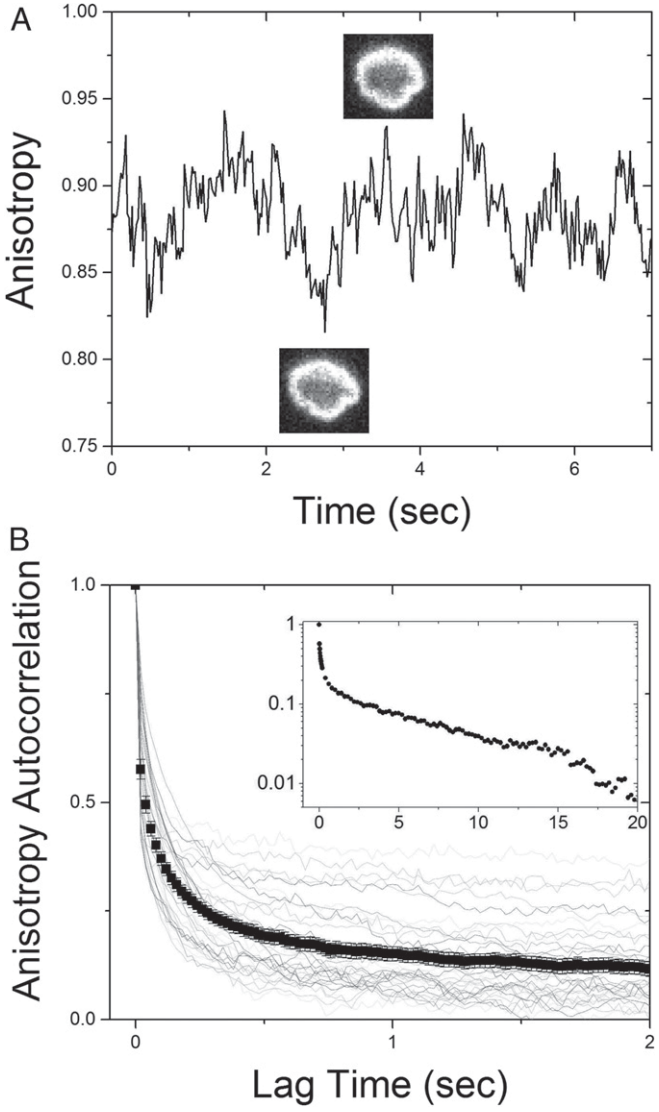

Fig. 4. (*A*) The anisotropy (ratio of minor and major planar axes) of a kinetoplast over time, with representative images of a local minimum and maximum. (*B*) Time autocorrelation function kinetoplast anisotropy showing the average curve over a population of kinetoplasts, each observed for 100 s at 50 frames per second. The autocorrelation function for each molecule is shown in gray. *Inset* shows the same data on a semilogarithmic axis over a longer time. The short timescale is 0.216 ± 0.004 s (SE), and the long timescale is 6.5 ± 0.1 s (SE).

(41–43). We examined the deformation response of kinetoplasts under weak confinement using microfluidic constrictions with a minimum width of 3.8 μm and a funnel-like entry that increases hyperbolically to a maximum width of 200 μm over a distance of 80 μm. The width of the channel, w, as a function of distance from where the constriction begins, x, can be described as $\mathrm{w(x)} = \frac{310\ \mu\mathrm{m}^2}{\mathrm{x}+1.55\ \mu\mathrm{m}}$. A bright-field image of the channel can be found in *SI Appendix*. Channels are 2 μm in depth (45). As the kinetoplasts approach the constriction, they are typically rotated by the funnel walls such that their major axis is aligned with the channel and are confined along their minor and transverse axes. Because most kinetoplasts have a minor axis greater than 3.8 μm, they fold or crumple to adapt to the constraints of the confinement and elongate along the channel axis. As the kinetoplasts leave the confining channel, they expand elastically back to their original equilibrium conformation.

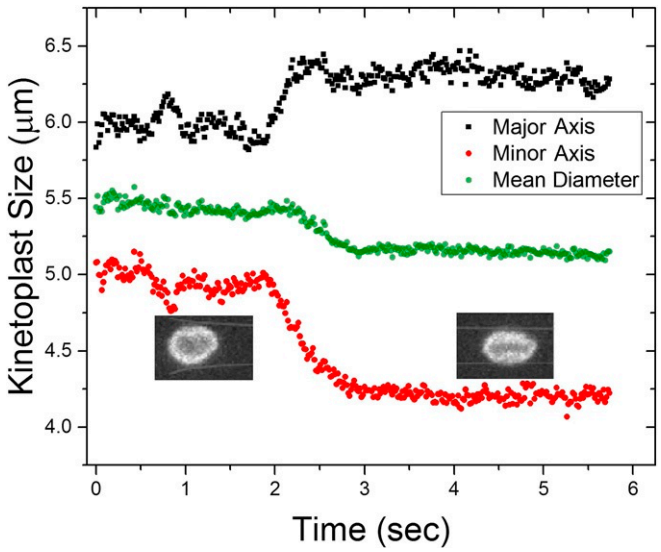

Fig. 5. Deformation of a kinetoplast entering a hyperbolic contraction with a terminal width of 3.8 μm. Major and minor axes of the kinetoplast are plotted over time as it enters the channel, showing the contraction of the minor axis and extension of the major axis, with representative images.

Fig. 5 shows the major and minor axes of a kinetoplast entering a confining channel, as the minor axis decreases by roughly 15% and the major axis elongates by roughly 5%. A parameter often used to characterize the extensibility of deformable objects in confinement is the deformation ratio, which is the ratio of the major axis to the width of the confining channel (41). The average deformation ratio of the ensemble of 18 confined kinetoplasts is 1.57 ± 0.02 (SE), slightly larger than the 1.1 to 1.2 measured for red blood cells in channels comparable with their size (41). Because there is a distribution of equilibrium anisotropies, we also report the lengthening coefficient, the deformation ratio divided by the equilibrium anisotropy, which is 1.23 ± 0.02 (SE). Histograms of both quantities are found in *SI Appendix*.

The specific deformation ratio that we measure is dependent on the channel size, which in this study, is only slightly smaller than a typical kinetoplast minor axis and is expected to increase in smaller channels. The topological constraints of the kinetoplast suggest that its extension in smaller channels is bounded, and future assays measuring the deformation–confinement relationship in the highly stretched limit may provide information about the elasticity of catenane bonds.

The hyperbolic entrance to the confining channel gives rise to an elongational electric field (44) that further deforms the kinetoplasts as they translate. When being driven toward the channel, the electric-field gradient compresses the kinetoplast perpendicular to the direction of motion and stretches it in this perpendicular direction as it leaves the channel. Similar transient effects at channel entrances have been seen in red blood cell constriction assays (41). The direction-dependent change in minor axis is not as drastic as that imposed by the confinement, but can be significant over repeated channel insertions and ejections of the same molecule. These asymmetric deformations, seen in *SI Appendix*, suggest future experiments for interrogating the elasticity of the kinetoplast sheet using extensional fields and flows.

Analogies may be made between kinetoplasts and lipid membranes based on the extensive literature on vesicle deformation (45, 46). Comparisons with vesicles are inherently qualitative due to the liquid nature of their surfaces. For example, a markedly different stretch response between polymerized and liquid sheets is predicted (47), but the relaxation dynamics are qualitatively similar. The bending modulus of an elastic sheet is related to its equilibration timescale such that the former can be estimated from the latter. A dimensional estimate for the relaxation timescale of a deformed vesicle presented by Zhou et al. (45) was derived as a balance of bending forces and viscosity. Equation 9 of Zhou et al. (45) relates the relaxation time τ, the solvent viscosity η, the bending rigidity κ, and the equilibrium radius r through $\tau = \frac{\eta r^3}{\pi\kappa}$. Using τ = 0.22 s, r = 5 μm, and η = 1 centipoise, we find $\kappa = 1.8 \times 10^{-19}$ J, comparable with experimental estimates of the bending rigidity of vesicles (47). Vesicles, while round at equilibrium, are known to deform into shapes that are akin to the harmonic modes that make up the PCs of kinetoplast shape (49). Because vesicles are nearly spherical at equilibrium, their shapes need not be described through PCA, but similar methods applied to living cell shapes (50) have found biological correlates to PC locations, suggesting experiments with living trypanosomes.

The most striking difference between one-dimensional (1D) and 2D polymers is that, while 1D polymers contract into a random coil to maximize entropy, the out-of-plane shape fluctuations that contribute to the conformational entropy of a 2D polymer are predicted to grow with a weaker scaling than the in-plane radius (51, 52), resulting in "flat" membranes with an infinite "persistence area." Despite the intrinsic curvature of kinetoplasts, this flatness phenomenon explains why they appear both smooth and stable. Indeed, the radii of gyration of duplicated kinetoplasts were found, based on the Pythagorean sum of the data in Fig. 2*B*, to be a factor of 1.4 ± 0.05 greater than the interphase kinetoplasts. This is consistent with the factor of $\sqrt{2}$ predicted for the flat phase, although further work is required to improve the precision of this measurement. The asymptotic smallness of transverse fluctuations is consistent with the low-amplitude shape variation that we observe over time and the comparatively fast timescale consistent with a highly restricted conformational space.

In future experiments, we envision exploring means to systematically tune the properties of kinetoplasts, which would enable investigation into topics of interest for 2D polymers. For example, the stiffness of the kinetoplast can be systematically modified through the removal of minicircles from the networks, either through the action of Topoisomerase II (31) or restriction enzymes (36), in sufficiently low concentrations such that the pattern of removed links does not percolate through the network. These partially decatenated kinetoplasts would maintain their overall shape but have a reduced areal density of links and thus, a lower bending rigidity. With these systems, we may be able to explore the crumpling transition that is predicted to occur when thermal fluctuations overcome bending rigidity (9). Alternatively, we can change the solvent quality in the experiments by using ethanol-based buffers (52), after which the kinetoplasts are expected to crumple through a process which is analogous to the coil-globule transition for 2D polymers (54). We also postulate that we can stiffen the kinetoplast network by effectively adding more cross-links, either through treatment of the system with Topoisomerase II in the presence of the anticancer drug ICRF-193 or replacing adenosine triphosphate (ATP) with a nonhydrolyzable analogue adenylyl-imidodiphosphate (AMP-PNP). In prior work, we have shown that these treatments inhibit topoisomerase-mediated strand passage and result in a persistent topoisomerase clamp between two DNA molecules (24).

In summary, our quantitative analysis of kinetoplasts under equilibrium and weak confinement conditions establishes their use as a model system to study the physics of elastic sheets and 2D polymers. Having imaged more extracellular kinetoplasts than any previous study, we find molecular individualism that

had not been appreciated, and our images and analysis suggest an increased role for the outer fibril in determining overall network structure, topology, and curvature. Our preliminary investigations into the deformation response of kinetoplasts suggest future investigations of kinetoplasts in complex flow to complement rheology studies of graphene oxide (55), and their 5-μm size makes them well suited for more detailed studies of microfluidic and nanofluidic confinement (13). Much like the first experiments with linear DNA that opened the door to a new field of single-polymer physics, we hope that kinetoplasts can serve a similar role for 2D systems.

Materials and Methods

C. fasciculata kinetoplasts were obtained from TopoGEN Inc. They were stained using the same protocol used to stain viral genomic DNA with a 8:1 base pair:dye ratio. In short, a solution was prepared consisting of 87.9% (vol/vol) 0.5× Tris-boric acid-ethylenediaminetetraacetic acid (TBE), 4% (vol/vol) beta-mercaptoethanol, 1.3% (vol/vol) YOYO-1 fluorescent dye at 10 μM, and 6.8% (vol/vol) kinetoplast DNA that had been diluted from stock to 10 μg/mL such that the stained solution contains 0.1 μg of DNA per 150-μL sample. While the kinetoplast DNA stains within seconds, standard procedure allows at least an hour of incubation to ensure uniform staining. The kinetoplast solution was either imaged under a microscope slide or in a 2-μm-high microfluidic channel, in which case 0.1% polyvinylpyrrolidone (10 kDa) solution was added to the buffer to prevent sticking and electroosmosis. While the diffusion of kinetoplasts is slow (taking several minutes to translate their own diameter), glycerol was added to the solution (77% vol/vol) to viscosify it and immobilize the kinetoplasts for confocal imaging, which was performed with a DeltaVision Elite Widefield Deconvolution microscope.

Microfluidic channels were made by pouring polydimethylsiloxane prepolymer onto a master silicon wafer containing features patterned in SU8 using photolithography. After annealing at 65 °C overnight, the cured PDMS was removed from the master wafer and cut into individual chips; then, holes were poked in each reservoir. The PDMS chips were cleaned by sonicating them in ethanol solution for 20 min and storing them overnight in TBE buffer to prevent permeation-driven flow. For experiments, chips were removed from the buffer, cleaned with water, dried, and placed onto a clean glass slide soaked previously in NaOH. DNA-containing buffer was pipetted into the reservoir hole of each device; then, platinum wires connected to a voltage supply were inserted. The voltage was activated to move the DNA into the field of interest within the device and stopped for imaging.

Kinetoplasts were imaged using a Zeiss Axiovert microscope with a 63× oil immersion lens (numerical aperture = 1.4), illuminated using a filtered light-emitting diode (ThorLabs), and recorded by a Photometrics 95B Prime CMOS camera interfaced with a computer using Micro-Manager (56). Images were analyzed using home-built MATLAB scripts. The 2 primary functions of the software were to calculate the gyration tensor and its eigenvectors and eigenvalues and to detect the edges and perform PCs analysis based on a population of detected edges. Both procedures are described in greater detail in *SI Appendix*, and the code is available on request.

Raw data in the form of microscopy videos in .tif format are available on the Harvard Dataverse public repository located at https://doi.org/10.7910/DVN/I4TWFV. Processed data used for the preparation of figures are in Dataset S1.

ACKNOWLEDGMENTS. This project was funded by NSF Grant CBET-1602406. B.W.S. is funded by the Agency for Science, Technology and Research, Singapore. We thank Dr. Wendy Salmon of the W. M. Keck Facility for Biological Imaging at the Whitehead Institute.

1. D. Akinwande *et al.*, A review on mechanics and mechanical properties of 2D materials-graphene and beyond. *Extreme Mech. Lett.* **13**, 42–77 (2017).
2. X. Zhuang, Y. Mai, D. Wu, F. Zhang, X. Feng, Two-dimensional soft nanomaterials: A fascinating world of materials. *Adv. Mater.* **27**, 403–427 (2015).
3. P. Payamyar, B. T. King, H. C. Oettinger, A. D. Schlüter, Two-dimensional polymers: Concepts and perspectives. *Chem. Commun.* **52**, 18–34 (2016).
4. F. Del Giudice, A. Q. Shen, Shear rheology of graphene oxide dispersions. *Curr. Opin. Chem. Eng.* **16**, 23–30 (2017).
5. A. B. Marciel, C. M. Schroeder, New directions in single polymer dynamics. *J. Polym. Sci. B Polym. Phys.* **51**, 556–566 (2013).
6. C. M. Schroeder, Single polymer dynamics for molecular rheology. *J. Rheol.* **62**, 371–403 (2018).
7. A. D. Schlüter, P. Payamyar, H. C. hristian Öttinger, How the world changes by going from one-to two-dimensional polymers in solution. *Macromol. Rapid Commun.* **37**, 1638–1650 (2016).
8. A. R. Koltonow, C. Luo, J. Luo, J. Huang, Graphene oxide sheets in solvents: To crumple or not to crumple? *ACS Omega* **2**, 8005–8009 (2017).
9. J. A. Aronovitz, T. C. Lubensky, Fluctuations of solid membranes. *Phys. Rev. Lett.* **60**, 2634–2637 (1988).
10. T. T. Perkins, D. E. Smith, S. Chu, Relaxation of a single DNA molecule observed by optical microscopy. *Science* **264**, 822–826 (1994).
11. T. T. Perkins, D. E. Smith, S. Chu, Direct observation of tube-like motion of a single polymer chain. *Science* **264**, 819–822 (1994).
12. E. S. G. Shaqfeh, The dynamics of single-molecule DNA in flow. *J. Non-Newtonian Fluid Mech.* **130**, 1–28 (2005).
13. L. Dai, C. B. Renner, P. S. Doyle, The polymer physics of single dna confined in nanochannels. *Adv. Colloid Interface Sci.* **232**, 80–100 (2016).
14. W. Reisner, J. N. Pedersen, R. H. Austin, DNA confinement in nanochannels: Physics and biological applications. *Rep. Prog. Phys.* **75**, 106601 (2012).
15. A. R. Klotz, H. W. de Haan, W. W. Reisner, Waves of DNA: Propagating excitations in extended nanoconfined polymers. *Phys. Rev. E* **94**, 042603 (2016).
16. Y. Li *et al.*, When ends meet: Circular DNA stretches differently in elongational flows. *Macromolecules* **48**, 5997–6001 (2015).
17. Y. Zhou *et al.*, Effect of molecular architecture on ring polymer dynamics in semidilute linear polymer solutions. *Nat. Commun.* **10**, 1753 (2019).
18. B. W. Soh, A. R. Klotz, R. M. Robertson-Anderson, P. S. Doyle, Long-lived self-entanglements in ring polymers. *Phys. Rev. Lett.* **123**, 048002 (2019).
19. D. J. Mai, A. B. Marciel, C. E. Sing, C. M. Schroeder, Topology-controlled relaxation dynamics of single branched polymers. *ACS Macro Lett.* **4**, 446–452 (2015).
20. A. R. Klotz, V. Narsimhan, B. W. Soh, P. S. Doyle, Dynamics of DNA knots during chain relaxation. *Macromolecules* **50**, 4074–4082 (2017).
21. A. R. Klotz, B. W. Soh, P. S. Doyle, Motion of knots in DNA stretched by elongational fields. *Phys. Rev. Lett.* **120**, 188003 (2018).
22. Q. Wu *et al.*, Poly [n] catenanes: Synthesis of molecular interlocked chains. *Science* **358**, 1434–1439 (2017).
23. B. A. Krajina, A. Zhu, S. C. Heilshorn, A. J. Spakowitz, Active DNA olympic hydrogels driven by topoisomerase activity. *Phys. Rev. Lett.* **121**, 148001 (2018).
24. Y. S. Kim *et al.*, Gelation of the genome by topoisomerase ii targeting anticancer agents. *Soft Matter* **9**, 1656–1663 (2013).
25. P. T. Englund, A passion for parasites. *J. Biol. Chem.* **289**, 33712–33729 (2014).
26. L. Simpson, J. Berliner, Isolation of the kinetoplast DNA of leishmania tarentolae in the form of a network. *J. Protozool.* **21**, 382–393 (1974).
27. D. Michieletto, "A bio-physical model for the kinetoplast DNA" in *Topological Interactions in Ring Polymers* (Springer, Basel, Switzerland, 2016), pp. 79–94.
28. D. Michieletto, D. Marenduzzo, E. Orlandini, Is the kinetoplast DNA a percolating network of linked rings at its critical point? *Phys. Biol.* **12**, 036001 (2015).
29. L. Ibrahim, P. Liu, M. Klingbeil, Y. Diao, J. Arsuaga, Estimating properties of kinetoplast DNA by fragmentation reactions. *J. Phys. A Math. Theor.* **52**, 034001 (2018).
30. A. R. Klotz, B. W. Soh, P. S. Doyle, Equilibrium Properties and Deformation Response of 2D Kinetoplast Sheets. Harvard Dataverse. https://doi.org/10.7910/DVN/I4TWFV. Deposited 6 November 2019.
31. T. Li, H. Zhang, L. Hu, F. Shao, Topoisomerase-based preparation and AFM imaging of multi-interlocked circular DNA. *Bioconjug. Chem.* **27**, 616–620 (2016).
32. M. Laurent, M. Steinert, Electron microscopy of kinetoplastic DNA from trypanosoma mega. *Proc. Natl. Acad. Sci. U.S.A.* **66**, 419–424 (1970).
33. M. M. Klingbeil, P. T. Englund, Closing the gaps in kinetoplast DNA network replication. *Proc. Natl. Acad. Sci. U.S.A.* **101**, 4333–4334 (2004).
34. R. Tibshirani, G. Walther, T. Hastie, Estimating the number of clusters in a data set via the gap statistic. *J. R. Stat. Soc. Ser. B* **63**, 411–423 (2001).
35. D. C. Barker, The ultrastructure of kinetoplast DNA with particular reference to the interpretation of dark field electron microscopy images of isolated, purified networks. *Micron* **11**, 21–62 (1980).
36. J. Chen, C. A. Rauch, J. H. White, P. T. Englund, N. R. Cozzarelli, The topology of the kinetoplast DNA network. *Cell* **80**, 61–69 (1995).
37. C.-C. Hsieh, A. Balducci, P. S. Doyle, An experimental study of DNA rotational relaxation time in nanoslits. *Macromolecules* **40**, 5196–5205 (2007).
38. W. Reisner *et al.*, Statics and dynamics of single DNA molecules confined in nanochannels. *Phys. Rev. Lett.* **94**, 196101 (2005).
39. D. J. Mai, C. Brockman, C. M. Schroeder, Microfluidic systems for single DNA dynamics. *Soft Matter* **8**, 10560–10572 (2012).
40. D. Gupta *et al.*, Mixed confinement regimes during equilibrium confinement spectroscopy of DNA. *J. Chem. Phys.* **140**, 214901 (2014).
41. D. Bento *et al.*, Deformation of red blood cells, air bubbles, and droplets in microfluidic devices: Flow visualizations and measurements. *Micromachines* **9**, 151 (2018).
42. A. M. Forsyth, J. Wan, W. D. Ristenpart, H. A. Stone, The dynamic behavior of chemically "stiffened" red blood cells in microchannel flows. *Microvasc. Res.* **80**, 37–43 (2010).
43. R. Haghgooie, M. Toner, P. S. Doyle, Squishy non-spherical hydrogel microparticles. *Macromol. Rapid Commun.* **31**, 128–134 (2010).
44. G. C. Randall, K. M. Schultz, P. S. Doyle, Methods to electrophoretically stretch DNA: Microcontractions, gels, and hybrid gel-microcontraction devices. *Lab Chip* **6**, 516–525 (2006).
45. H. Zhou, B. B. Gabilondo, W. Losert, W. van de Water, Stretching and relaxation of vesicles. *Phys. Rev. E* **83**, 011905 (2011).

46. K. Liu *et al.*, Dynamics of a multicomponent vesicle in shear flow. *Soft Matter* **13**, 3521–3531 (2017).
47. O. Rossier *et al.*, Giant vesicles under flows: Extrusion and retraction of tubes. *Langmuir* **19**, 575–584 (2003).
48. M. Yu, R. B. Lira, K. A. Riske, R. Dimova, H. Lin, Ellipsoidal relaxation of deformed vesicles. *Phys. Rev. Lett.* **115**, 128303 (2015).
49. F. Quemeneur, C. Quilliet, M. Faivre, A. Viallat, B. Pépin-Donat, Gel phase vesicles buckle into specific shapes. *Phys. Rev. Lett.* **108**, 108303 (2012).
50. L. Tweedy, B. Meier, J. Stephan, D. Heinrich, R. G. Endres, Distinct cell shapes determine accurate chemotaxis. *Sci. Rep.* **3**, 2606 (2013).
51. Y. Kantor, D. R. Nelson, Crumpling transition in polymerized membranes. *Phys. Rev. Lett.* **8**, 2774 (1987).
52. Y. Kantor, D. R. Nelson, Phase transitions in flexible polymeric surfaces. *Phys. Rev. A* **36**, 4020–4032 (1987).
53. L. Dai, J. J. Jones, A. R. Klotz, S. Levy, P. S. Doyle, Nanoconfinement greatly speeds up the nucleation and the annealing in single-DNA collapse. *Soft Matter* **13**, 6363–6371 (2017).
54. F. F. Abraham, M. Kardar, Folding and unbinding transitions in tethered membranes. *Science* **252**, 419–422 (1991).
55. A. Corker, H. C.-H. Ng, R. J. Poole, E. García-Tuñón, 3d printing with 2d colloids: Designing rheology protocols to predict 'printability'of soft-materials. *Soft Matter* **15**, 1444–1456 (2019).
56. A. D. Edelstein *et al.*, Advanced methods of microscope control using μmanager software. *J. Biol. Methods* **1**, e10 (2014).